

# Rotating azimuthons in dissipative Kerr media excited by superpositions of Bessel beams

Carlos Ruiz-Jiménez<sup>1</sup>, Hervé Leblond<sup>2</sup>, Miguel A. Porrás<sup>1</sup>, and Boris A. Malomed<sup>3,4</sup>

<sup>1</sup>*Grupo de Sistemas Complejos, ETSIME, Universidad Politécnica de Madrid, Ríos Rosas 21, 28003 Madrid, Spain*

<sup>2</sup>*Laboratoire de Photonique d'Angers, EA 4464, Université d'Angers, 2 Bd Lavoisier, 49000 Angers, France*

<sup>3</sup>*Department of Physical Electronics, School of Electrical Engineering, Faculty of Engineering, and Center for Light-Matter interaction, Tel Aviv University, Tel Aviv 69978, Israel and*

<sup>4</sup>*Instituto de Alta Investigación, Universidad de Tarapacá, Casilla 7D, Arica, Chile*

We report the existence of persistently rotating azimuthons in media with self-focusing Kerr and absorption nonlinearities. The nonlinear loss is balanced by power influx from the peripheral reservoir stored in a slowly decaying tail of the field. The azimuthon modes are excited by a superposition of two Bessel beams with opposite vorticities,  $\pm s$ , and slightly different conicities. The excited mode exhibits vorticity in its center opposite to that of the input Bessel-beam superposition, due to spontaneous inversion of the topological charge in the course of the azimuthon formation. Unlike azimuthons in loss-free media, number  $N$  of rotating intensity maxima and  $s$  are not mutually independent, being related by  $N = 2s$ . The robustness of the rotating azimuthons is enhanced in comparison to similar static dissipative patterns. They can be excited in almost any transparent material, in the range of intensities for which the nonlinear absorption, induced by multiphoton absorption, is relevant. Close to the ionization threshold, the rotating azimuthons are similar to recently observed helical filaments of light in air and CS<sub>2</sub>.

## I. INTRODUCTION

Solitons, solitary vortices [1, 2], necklace-shaped clusters [3, 4], and azimuthons [5, 6] are increasingly sophisticated, self-trapped light modes in nonlinear optical media, which have been predicted and experimentally realized in the course of the last decades [7]. In particular, soliton clusters and azimuthons feature propagation-invariant or nearly-invariant intensity patterns that rotate uniformly as they propagate in transparent media, and require a stabilizing mechanism to arrest the collapse instability brought by the self-focusing Kerr nonlinearity. Such a mechanism may be provided by saturation of the Kerr nonlinearity [3, 5, 8]. Many of these solitary structures have dissipative-soliton counterparts, which are supported by the balance between gain and losses, which occurs in laser cavities, in addition to the balance between the diffraction and self-focusing [9–12].

Relaxing the condition of strong localization, one can consider weakly localized states similar to Bessel beams [13–15], whose total norm (integral power, in terms of optics) diverges at  $r \rightarrow \infty$ , where  $r$  is the radial coordinate in the two-dimensional plane, perpendicular to the propagation axis,  $z$ . Unlike dissipative solitons, stationarity of such states is supported not through the balance of loss and gain, but rather due to the compensation of nonlinear dissipation, induced by multiphoton absorption in the optical material (which may generate weak plasma) and influx of power stored, in an indefinitely large (diverging) amount, in the weakly decaying tail of the quasi-Gaussian beam [13–16].

Similarly to the above-mentioned conservative systems, nonlinear dissipative Bessel beams with embedded vorticity have been predicted [17, 18], and experimentally observed to induce tubular filamentation [19]. A remarkable fact is that the dissipative nonlinear Bessel

vortex beams can be stable in self-focusing media with the pure-cubic (Kerr) nonlinearity due to the stabilizing action of the nonlinear absorption [20]. More recently, launching arbitrary superpositions of Bessel beams with the same cone angle but different embedded vorticities has been shown to excite propagation-invariant (stationary) dissipation patterns of rather arbitrary shapes, the so-called “dissipatons” [21].

In this work, which is motivated, in part, by recent experiments exhibiting helical filamentation of light beams [22, 23], we predict the existence of what we call *rotating dissipative azimuthons*. These modes propagate steadily, with a constant rotation velocity, in nonlinearly absorbing Kerr media, being excited by superpositions of two Bessel vortex beams with opposite vorticities and slightly different conicities. Such coherent superpositions of Bessel beams can be readily generated in the experiment. In the linear approximation, their propagation was theoretically studied in Refs. [24–26].

Unlike soliton clusters and azimuthons in conservative systems, number  $N$  of rotating high-intensity peaks (“hot spots”) and vorticity  $s$  at the center of the dissipative azimuthon are not independent integers, but are related by  $N = 2s$ , which can be explained analytically (see below). The rotating azimuthons exhibit a mixed linear-nonlinear behavior, resembling in some aspects the linear propagation of superpositions of Bessel beams with opposite vorticities and different cone angles, while in other respects they are similar to solitons clusters. Namely, their quasi-linear peripheral field imposes the same angular velocity of rotation as that induced by the Bessel-beam superposition, see Eq. (6) below. However, the vorticity at the center of the azimuthon acquires a topological charge *opposite* to that of the input superposition of the Bessel wave functions, as a result of the topological-charge inversion in the course of the formation of the azimuthon,

which can be explained by a trend to minimization of the Hamiltonian of the model's conservative part. As a result, the dissipative azimuthon rotates in the direction opposite to the azimuthal gradient of the phase associated with the vorticity at the center, in the same way as soliton clusters do.

We also report a gyroscopic effect in the spontaneous formation of dissipative azimuthons, *viz.*, that the rotation accelerates the formation of the spinning steady-shape patterns, in comparison to similar non-rotating steady ones (“dissipatons”), which arise when cone angles of the two Bessel beams are equal in the input state. We also observe enhanced stability of the rotating dissipative azimuthons, as compared to dissipative Bessel vortex beams and static dissipatons. In the case of instability, the rotating dissipatons feature richer dynamics, including formation of persistently pulsating azimuthons.

Basic results, produced by systematic numerical simulations of the model, are reported in Section II. The gyroscopic effect and a detailed analysis of the stability of the rotating dissipative azimuthons are presented in Section III and IV, respectively. The paper is concluded by Section V, while Appendix presents specific details of the numerical algorithms used in the paper.

## II. DISSIPATIVE AZIMUTHONS EXCITED BY SUPERPOSITIONS OF BESSEL BEAMS WITH OPPOSITE TOPOLOGICAL CHARGES

We consider the propagation of monochromatic light beams along the  $z$  axis,  $E = A \exp(-i\omega t + ikz)$ , with carrier frequency  $\omega$  and propagation constant  $k = n\omega/c$ , where  $c$  is the speed of light in vacuum, and  $n$  is the linear refractive index. The nonlinear Schrödinger equation (NLSE) that governs the paraxial propagation of field envelope  $A$ , is [17]

$$\partial_z A = \frac{i}{2k} \nabla_{\perp}^2 A + \frac{ikn_2}{n} |A|^2 A - \frac{\beta^{(M)}}{2} |A|^{2M-2} A, \quad (1)$$

where  $\nabla_{\perp}^2 \equiv \partial_r^2 + (1/r)\partial_r + (1/r^2)\partial_{\varphi}^2$  is the transverse Laplacian, which is here written in polar coordinates  $(r, \varphi)$  in the transverse plane (all simulations were performed, in parallel, in both the Cartesian and polar coordinates, see Appendix),  $n_2 > 0$  is the nonlinear refractive index, and  $\beta^{(M)} > 0$  is the multiphoton absorption coefficient of order  $M$ .

In the context of filamentation, one can consider a more accurate model in which  $A$  is a function of time, and including material dispersion for pulsed beams, and plasma-defocusing effects. Actually, the material dispersion may be neglected for propagation distances smaller than the dispersion length, as confirmed by the theoretical and experimental studies of the filamentation with Bessel beams [18, 19]. In terms of our simulations displayed in Figs. 1 and 2, dispersion effects in air would become relevant at the dispersion length  $z \approx 250$  m for typical pulses with temporal duration 100 fs. Therefore, the

dispersion is negligible for distances of  $\approx 1$  m presented in this work. In particular, it was theoretically and experimentally shown that the filamentation dynamics of Bessel beams is correctly captured by the monochromatic model with  $A$  multiplied by an invariant temporal pulse shape, as the key ingredients which determine the filamentation are diffraction, Kerr self-focusing, and multiphoton absorption, while plasma defocusing plays a secondary role [18, 19].

In the absence of the Kerr and multiphoton absorption terms, Eq. (1) is satisfied by Bessel beams carrying vorticity with any integer topological charge  $s$ . In the form explicitly representing the paraxial approximation, they are  $A(r, \varphi) \propto J_s(k\theta_s r) \exp(is\varphi) \exp(i\delta_s z)$ , where  $J_s$  is the Bessel function of order  $s$ ,  $\theta_s > 0$  is the cone angle, and

$$\delta_s = -k\theta_s^2/2 < 0 \quad (2)$$

is the contribution to the propagation constant associated with the conical geometry of the Bessel beam. In the linear regime, Eq. (1) is actually satisfied by any superposition of Bessel beams with arbitrary topological charges, amplitudes and cone angles. In particular, superpositions with different cone angles produce propagation-invariant intensity patterns which rotate in the course of the propagation [24, 25]. Rotatory polarization patterns in free space, emulating optical activity of the effective medium, have also been demonstrated in superpositions of orthogonally polarized Bessel beams with different cone angles [26].

In nonlinear regimes, starting from Refs. [27] for the pure-Kerr medium, and [13, 14] which included more general nonlinearities and dissipative nonlinear terms, undistorted and inattenuated propagation in the form of nonlinear Bessel beams was demonstrated experimentally. A linear Bessel beam launched in the nonlinear medium spontaneously transforms into an appropriately deformed beam. Subsequently, similar results have been demonstrated for vortical Bessel beams, which too were shown to transform into propagation-invariant nonlinear counterparts [17–19]. The existence of fully stable nonlinear Bessel vortex beams in media with pure-cubic Kerr nonlinearity has been established in Ref. [20], where the stabilizing mechanism was provided by nonlinear absorption. In a more recent study, arbitrary superpositions of Bessel beams with different topological charges and amplitudes but identical cone angles, launched into the medium with nonlinear absorption [21], were shown to excite propagation-invariant “dissipatons”, which are nearly arbitrary structures composed of vortices and bright spots where the power is continuously dissipated. In those studies, stationarity propagation in media with nonlinear absorption was enabled by a feeding mechanism provided by power influx from the reservoir with an indefinitely large capacity, maintained by the slowly decaying quasi-linear tails of nonlinear Bessel vortex beams and dissipatons. This mechanism is not possible for strongly localized dissipative solitons with convergent in-

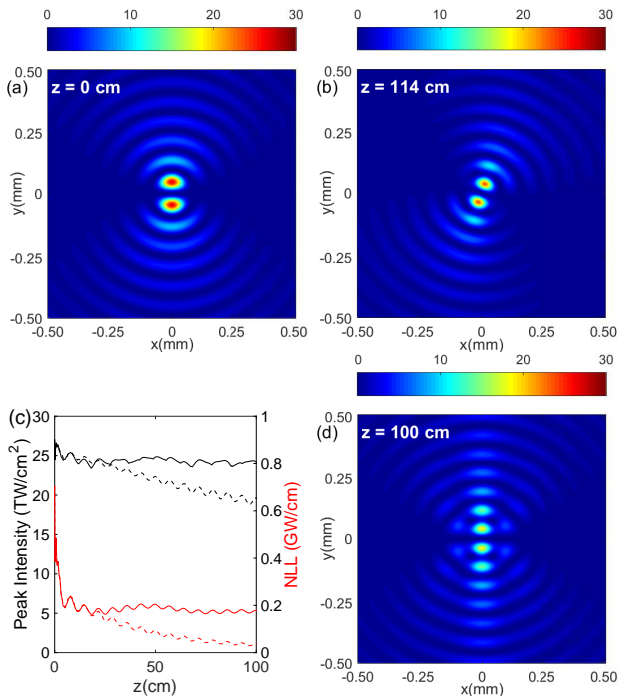


FIG. 1. Results of simulations of Eq. (1) with parameters corresponding to the high-intensity light propagation in air at the carrier wavelength 800 nm ( $n \approx 1$ ,  $n_2 = 3.2 \times 10^{-19}$  cm<sup>2</sup>/W,  $M = 8$ ,  $\beta^{(8)} = 1.8 \times 10^{-94}$  cm<sup>13</sup>/W<sup>7</sup> [16]). (a) The input intensity profile, given by Eq. (3), and measured in units of TW/cm<sup>2</sup>, with  $s = 1$ ,  $\theta_1 = 0.25^\circ$ ,  $\theta_{-1} = 0.26^\circ$ , and  $a_1^2 = 20$  TW/cm<sup>2</sup> (the respective peak intensity is 27.04 TW/cm<sup>2</sup>). The corresponding scaled parameters in Eqs. (10) and (14) are  $M = 8$ ,  $\alpha = 0.85$ , and  $\eta = -0.02$ ,  $b_1 = 0.87$ . (b) The transverse intensity profile of the quasi-stationary rotating azimuthon, measured at the propagation distance  $z = 114$  cm (the peak intensity of the profile is 24.25 TW/cm<sup>2</sup>). Numerical evaluation of its angular velocity yields  $\Omega = -1.75 \pm 0.01$  deg/cm, with the sign corresponds to the clockwise direction. This value is in close agreement with  $\Omega = -1.758$  deg/cm given by Eq. (6) from the linear theory. (c) The nearly constant peak intensity and NLL (the nonlinear-loss rate), defined as per Eq. (7) (black and red continuous lines), vs. the propagation distance,  $z$ . Dashed lines represent a non-rotating pattern for the same parameters, except that the two cone angles are equal to  $0.255^\circ$ . (d) The corresponding static pattern ( $\Omega = 0$ ), not yet completely formed, at  $z = 100$  cm.

tegral power, that should be maintained by intrinsic gain.

Searching for steady states in the rotating frame, we look for solutions to Eq. (1) with input

$$A(r, \varphi, z = 0) = a_s [J_s(k\theta_s r) \exp(is\varphi) + J_{-s}(k\theta_{-s} r) \exp(-is\varphi)], \quad (3)$$

composed of two Bessel beams with equal amplitudes  $a_s$ , opposite vorticities  $\pm s$ ,  $s = 1, 2, \dots$  and slightly different cone angles,  $\theta_{\pm s} > 0$ , hence the respective shifts of the axial wave vectors,

$$\delta_{\pm s} = -k\theta_{\pm s}^2/2, \quad (4)$$

are slightly different too. It is worthy to note that the solution of the linearized version of Eq. (1) seeded by input (3), namely,

$$A(r, \varphi, z) = a_s [J_s(k\theta_s r) \exp(is\varphi + i\delta_s z) + J_{-s}(k\theta_{-s} r) \exp(-is\varphi + i\delta_{-s} z)], \quad (5)$$

features vorticity  $s$  at its center ( $r \rightarrow 0$ ) for  $\theta_s > \theta_{-s}$ , and  $-s$  for  $\theta_s < \theta_{-s}$ , with counterclockwise and clockwise phase circulation,  $\pm 2\pi s$ , respectively, along a circle of small radius  $r$ . With increasing radius, the vorticity keeps switching between  $s$  to  $-s$ . The angular velocity of the rotation of the intensity pattern,  $|A(r, \varphi, z)|^2$ , corresponding to the linear solution in Eq. (5) is [24, 25]

$$\Omega = \frac{\delta_{-s} - \delta_s}{2s} = \frac{k}{4s} (\theta_s^2 - \theta_{-s}^2), \quad (6)$$

where Eq. (4) is used, which is counterclockwise (positive) for  $\theta_s > \theta_{-s}$  and clockwise (negative) for  $\theta_s < \theta_{-s}$ . Thus, the direction of the rotation of the intensity pattern coincides with the direction of the azimuthal gradient of the phase close to the beam's center in these linear superpositions of Bessel beams.

Figure 1(a) displays an example of the nonlinear evolution produced by initial condition in Eq. (3) with  $s = 1$  and slightly different cone angles. The simulations of Eq. (1) were performed (as mentioned above, in both Cartesian and polar coordinates) with parameters corresponding to the propagation of high-intensity light in air, in the regime for which the Kerr self-focusing and nonlinear absorption are significant (see the caption to the figure for details). The numerical solution demonstrates that the propagating beam quickly attains a steady rotatory state, featuring compressed lobes as a result of the Kerr self-focusing, as seen in Fig. 1(b). The solid black curve in Fig. 1(c) shows that the peak intensity approaches a constant value in the course of the propagation, confirming the stationarity of the rotating pattern. Another manifestation of the steady propagation is the fact that the rate of the nonlinear loss (NLL) of the power,

$$\text{NLL} = 2\pi\beta^{(M)} \int_0^\infty |A(r)|^{2M} r dr, \quad (7)$$

also attains a nearly constant value, as shown by the red solid curve in Fig. 1(c). Thus, the rotating structure is a genuine dissipative azimuthon.

As shown in Figs. 1-5 for different values of  $s$ , intensity patterns of dissipative azimuthons preserve the  $2s$ -fold rotational symmetry of the input configuration given by Eq. (3). Thus, the number of “hot spots” in the rotating azimuthons,  $N = 2s$ , is only determined by magnitude  $s$  of the topological charge in the two beams which build the input. In this respect, dissipative azimuthons differ from their conservative counterparts and soliton clusters, for which the number of hot spots and the vorticity at the center are independent integers [5, 6]. The latter property of the conservative model is explained by the

fact that the number of intensity maxima in the circular pattern is determined by the modulational instability of the axially uniform state.

Another manifestation of the robustness of the dissipative azimuthons is that they preserve the angular velocity imposed by the superposition of the two vortex Bessel beams in input (3), *viz.*,  $\Omega = (\delta_{-s} - \delta_s)/2s$ ; hence the rotation period is  $z_{\text{rotation}} = 4\pi s/|\delta_{-s} - \delta_s|$ , and, given the 2s-fold rotational symmetry of the rotating pattern, it periodically repeats itself after passing distance  $2\pi/|\delta_{-s} - \delta_s|$ , independent of the topological charge,  $s$ . The preservation of the angular velocity is explained by the fact that the dissipative azimuthon is surrounded by the quasi-linear asymptotic field (providing the above-mentioned power reservoir) that continues to rotate as the input linear superposition does, *i.e.*, with angular velocity (6). Since the whole structure is stationary in the rotating frame, the inner nonlinear region rotates synchronously with the small-amplitude periphery.

A general feature of dissipative azimuthons that makes them substantially different from the linear Bessel superposition in Eq. (5) is that the direction of rotation of the intensity pattern is *opposite* to the direction of the azimuthal phase gradient close to the pattern's pivot. The reason is that the topological charge of the vortex at the center reverses its sign in the course of the azimuthon formation from the initial Bessel beam superposition, as shown in Fig. 2. The intensity pattern of the input Bessel-beam superposition in Fig. 2(a) has  $\theta_s > \theta_{-s}$ , hence the input vorticity at the center is  $s = 1$ , corresponding to the counterclockwise phase increase by  $2\pi s$  around the origin, as shown by the azimuthal phase profile in Fig. 2(c). Accordingly, the intensity pattern in the azimuthon established by the evolution of the intensity pattern, which is displayed in Fig. 2(b), rotates counterclockwise too. However, the vorticity at the center inverts in the course of the evolution to  $-s = -1$ , corresponding to the clockwise phase circulation  $2\pi s$  around the origin, as seen in Fig. 2(d). Details of the transformation of the azimuthal phase profile from vorticity  $s = 1$  in Fig. 2(c) to  $-s = -1$  in Fig. 2(d) in the course of the formation of the azimuthon are shown in Supplemental Material [URL of Fig2cd.avi]. The vorticity inversion affects the entire central zone of the azimuthon, including the hot spots. At larger radii the vorticity oscillates, and in the peripheral zone the periodic alternations coincide with those of the input Bessel-beam superposition.

It is relevant to note that a possibility of the dynamical inversion of the sign of the topological charge of an optical vortex in a conservative medium, which interacts with a material lattice structure, was previously predicted theoretically [28] and demonstrated experimentally [29]. In the present setting, the rotating intensity pattern emerging in the azimuthon mode may play a role of such a lattice. Indeed, the rotation of a layer with radius  $R$  at angular velocity  $\Omega$  tends to add the term generated by the Galilean transform,  $kR^2\Omega(\varphi - \Omega z/2)$ , to the phase of the wave field (subject to the periodicity constraint,

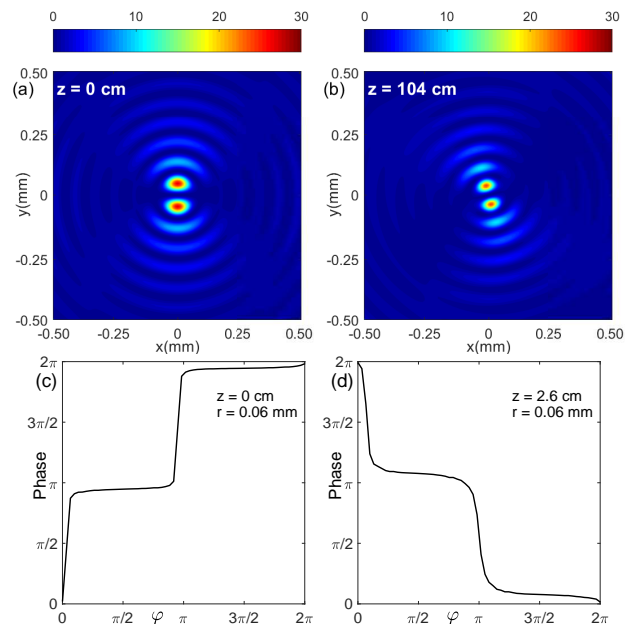


FIG. 2. Results for the setting with the same parameters as in Fig. 1. (a) The transverse intensity profile, measured in  $\text{TW}/\text{cm}^2$ , of the superposition of the Bessel beams in the input given by Eq. (3), with  $s = 1$ ,  $\theta_1 = 0.26^\circ$ ,  $\theta_{-1} = 0.24^\circ$ , and  $a_1^2 = 20 \text{ TW}/\text{cm}^2$ . The corresponding scaled parameters in equations (10) and (14) are  $M = 8$ ,  $\alpha = 0.88$ , and  $\eta = 0.04$ ,  $b_1 = 0.87$ , respectively. (b) The intensity profile of the azimuthon produced by the propagation over distance  $z = 100 \text{ cm}$ . The counterclockwise angular velocity is  $\Omega = 3.40 \pm 0.08 \text{ deg}/\text{cm}$  from the numerical simulations and  $\Omega = 3.447 \text{ deg}/\text{cm}$  from Eq. (6). See Supplemental Material at [URL of Fig2ab.avi] for the excitation of the azimuthon from (a) to (b). Panels (c) and (d) display the azimuthal phase profiles along a circle of small radius  $r$  for the input Bessel-beam superposition (3), and for the azimuthon established by the propagation, respectively. See Supplemental Material at [URL of Fig2cd.avi] for the transformation from (c) to (d) in the course of the propagation, with the phase unwrapped in  $[0, 2\pi]$ .

$kR^2\Omega = m$ , with integer  $m$ ). If, on the other hand, vorticity phase  $\pm s\varphi$  dominates at  $r$  small enough, the minimization of the gradient term in the Hamiltonian of the conservative part of Eq. (1), with density  $(2k)^{-1} |\nabla_{\perp} A|^2$ , suggests to choose mutual signs of  $\Omega$  and  $s$  which help to cancel different contributions to the phase.

Thus, dissipative azimuthons clearly exhibit a mixed linear-nonlinear structure: The stationary intensity pattern, including the quasi-linear periphery, rotating with angular velocity given by Eq. (6), which is imposed by input (3), and a restructured nonlinear core, including the circular chain of hot spots, whose vorticity is inverted with respect to the rotation direction, as in soliton clusters [3, 5].

For a more comprehensive study of properties of the dissipative azimuthons [in particular, their (in)stability],

we introduce

$$\delta \equiv \frac{1}{2} (\delta_s + \delta_{-s}), \quad \Delta\delta \equiv \frac{1}{2} (\delta_s - \delta_{-s}), \quad (8)$$

where  $\delta_{\pm s}$  is defined as per Eq. (2), and the scaled radius and propagation distance,

$$\rho \equiv \sqrt{2k|\delta|r}, \quad \zeta \equiv |\delta|z, \quad \tilde{A} \equiv \left( \frac{\beta^{(M)}}{2|\delta|} \right)^{\frac{1}{2M-2}} A. \quad (9)$$

These rescalings transform NLSE (1) into

$$\partial_{\zeta} \tilde{A} = i \nabla_{\perp}^2 \tilde{A} + i \alpha |\tilde{A}|^2 \tilde{A} - |\tilde{A}|^{2M-2} \tilde{A}, \quad (10)$$

where now  $\nabla_{\perp}^2 = \partial_{\rho}^2 + (1/\rho)\partial_{\rho} + (1/\rho^2)\partial_{\varphi}^2$ , and

$$\alpha \equiv \left( \frac{2|\delta|}{\beta^{(M)}} \right)^{1/(M-1)} \frac{kn_2}{n|\delta|}. \quad (11)$$

In this notation, input (3) takes the form of

$$A(\rho, \varphi, 0) = b_s \left[ J_s \left( \sqrt{1 + \frac{\Delta\delta}{\delta}} \rho \right) e^{is\varphi} + J_{-s} \left( \sqrt{1 - \frac{\Delta\delta}{\delta}} \rho \right) e^{-is\varphi} \right], \quad (12)$$

which, given the smallness of  $|\Delta\delta/\delta|$  for close values of the cone angles, may be approximated by

$$A(\rho, \varphi, 0) = b_s \left[ J_s((1+\eta)\rho) e^{is\varphi} + J_{-s}((1-\eta)\rho) e^{-is\varphi} \right], \quad (13)$$

where we set  $\sqrt{1 \pm \Delta\delta/\delta} \simeq 1 \pm \eta$ , and

$$\eta \equiv \frac{\Delta\delta}{2\delta}, \quad b_s \equiv \left( \frac{\beta^{(M)}}{2|\delta|} \right)^{\frac{1}{2M-2}} a_s. \quad (14)$$

Properties of dissipative azimuthons, similar to what was previously reported for static dissipations and nonlinear Bessel vortex beams, are essentially the same, regardless of the multiphoton absorption order  $M$  in Eq. 3, therefore we henceforth fix  $M = 4$  (note, in particular, that  $M = 4$  takes place in water at 527 nm). The dissipative azimuthon is then determined by vorticity  $s$ , the strength of the Kerr nonlinearity relative to the nonlinear absorption,  $\alpha$ , the amplitude parameter,  $b_s$ , and the radial mismatch,  $\eta$  of the input Bessel beams, see Eqs. (11) and (14). Positive and negative  $\eta$  correspond, respectively, to  $\theta_s > \theta_{-s}$  and  $\theta_s < \theta_{-s}$ , i.e., positive (counterclockwise) and negative (clockwise) angular velocity. In the scaled notation, the angular velocity is

$$\varpi = \frac{2\eta}{s}, \quad (15)$$

and the rotation period is  $\zeta_{\text{rotation}} = \pi s/|\eta|$ . The above-mentioned inversion of the vorticity implies that the respective topological charges are  $-s$  and  $s$  for  $\eta > 0$  and  $\eta < 0$ , respectively. STOP

### III. THE GYROSCOPIC EFFECT IN DISSIPATIVE AZIMUTHONS

In comparison to nonlinear Bessel beams and static dissipatons [17, 21], it is seen in Figs. 1 and 3 that the rotation accelerates the formation of the dissipative patterns. The dashed curves in Fig. 1(c) show the peak intensity and nonlinear power loss rate as functions of the propagation distance, and Fig. 1(d) displays the static intensity pattern established, after some propagation distance, in the nonlinear medium, when the cone angles of the input Bessel beams are made equal to the mean value of the two slightly different angles of the original input. It is seen that the profile with the equal conicities is not yet formed because it still continues to decrease its amplitude, in comparison to the original one that propagates without attenuation. The non-rotating pattern requires a much longer propagation distance to form than its steadily rotating counterpart, whose formation is promoted by what may be called a *gyroscopic effect*. Namely, if the static pattern is created by input (13) with  $\eta = 0$ , the slow relaxation towards the static state is characterized by a certain relaxation length,  $\zeta_{\text{rel}}$ .

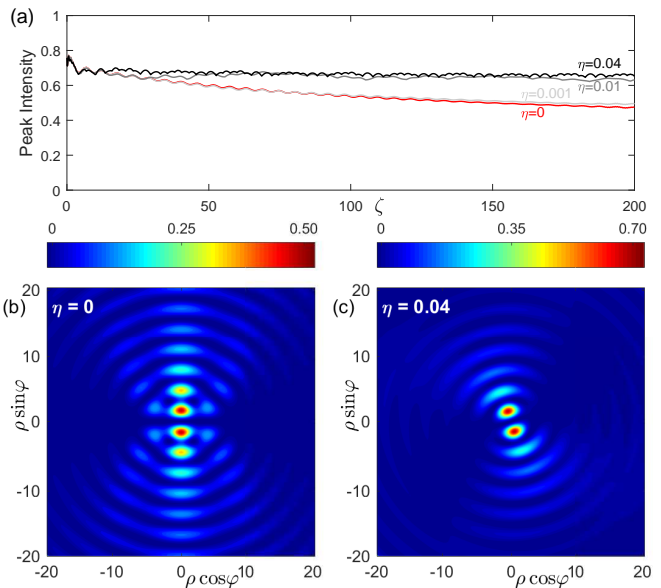


FIG. 3. (a) Peak intensities as functions of the propagation distance for the dissipative azimuthons formed, at values of parameters  $M = 4$ ,  $\alpha = 1$ , starting with the Bessel-beam superposition input given by Eq. (13), with  $s = 1$ ,  $b_1 = 0.75$  and increasing values of scaled mismatch,  $\eta = 0, 0.001, 0.01$  and  $0.04$ , see Eq. (14). The characteristic relaxation distance for  $\eta = 0$  is  $\zeta_{\text{rel}} \simeq 70$ , yielding  $|\eta|_{\text{min}} \simeq 0.04$ , see Eq. (16). (b) The intensity pattern of the non-rotating dissipaton formed with  $\eta = 0$  and  $\varpi = 0$ . (c) The same as in (b) but for the rotating dissipative azimuthon with  $\eta = 0.04$  and counterclockwise scaled angular velocity,  $\varpi = 0.081 \pm 0.003$  as obtained from the simulations, and  $\varpi = 0.080$ , as produced by Eq. (15). The latter pattern forms after propagating a much shorter distance.

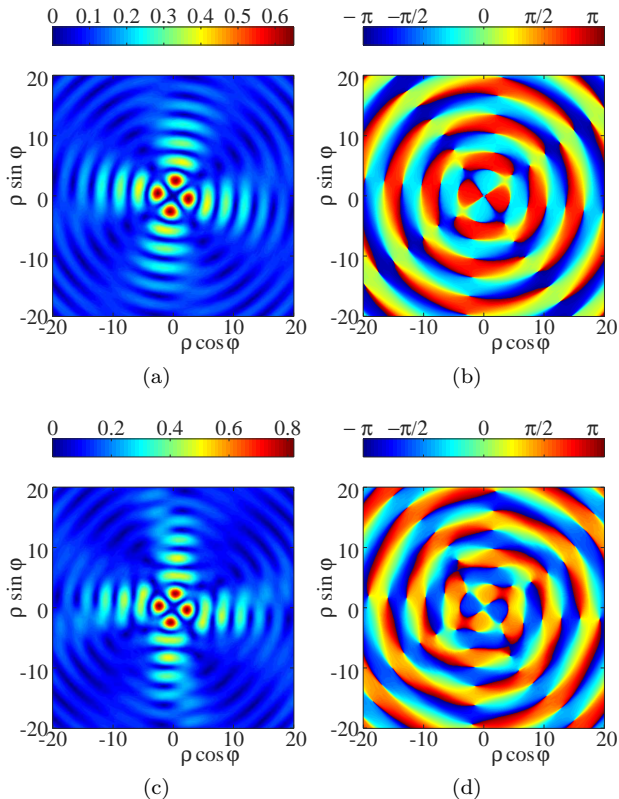


FIG. 4. Stable dissipative azimuthons, spontaneously formed, in the setting with  $M = 4$  and Kerr coefficient  $\alpha = 1.8$ , from input (3) with  $s = 2$  and  $\eta = 0.04$ . (a) The amplitude and (b) phase profiles at  $\zeta = 270$ , obtained starting with the scaled Bessel amplitude  $|b_s| = 0.6$ . The angular velocity is  $\varpi \simeq 0.0403 \pm 0.0002$ , while  $2\eta/s = 0.04$ , see Supplemental Material [URL of Fig4a.avi] for the excitation of the azimuthon in (a) from the input Bessel-beam superposition. Panels (c) and (d) display the same as (a) and (b), but for  $\alpha = 2$  and  $|b_s| = 0.8$ , the angular velocity being  $\varpi \simeq 0.0403 \pm 0.0004$ .

On the other hand, if slight difference of conicities of the two Bessel beams in the input promotes the formation of a steadily rotating state, characterized by a rotation period  $\zeta_{\text{rotation}} = \pi s/|\eta|$ . The rotation is expected to eclipse the slow relaxation provided that  $\zeta_{\text{rotation}} \lesssim \zeta_{\text{rel}}$ , i.e., for

$$|\eta| \gtrsim |\eta|_{\text{min}} = \pi s/\zeta_{\text{rel}}. \quad (16)$$

In the example displayed Fig. 3 with  $s = 1$ ,  $b_1 = 0.75$  and  $M = 4$ ,  $\alpha = 1$ , the characteristic relaxation distance,  $\zeta_{\text{rel}} \sim 70$ , of the non-rotating pattern predicts  $|\eta|_{\text{min}} \simeq 0.04$ . As seen in Fig. 3(a), the long relaxation stage, following the short initial stage of compression under the combined action of the self-focusing and absorption, is indeed eliminated at  $\eta \gtrsim |\eta|_{\text{min}}$ . Eventually, the snapshot of the intensity pattern in the rotating state is quite similar to that of the non-rotating one, cf. Figs. 3(b) and (c), but the rotating pattern forms much faster.

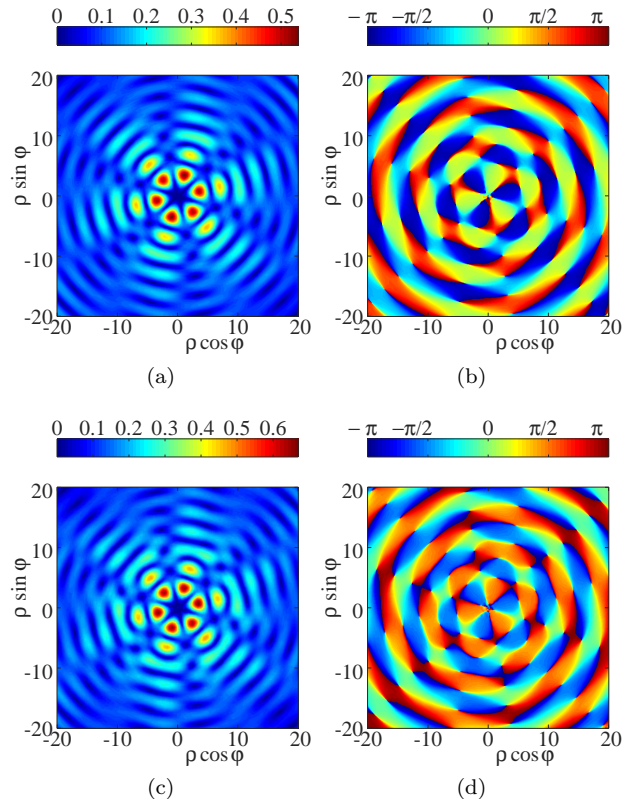


FIG. 5. Stable dissipative azimuthons established in the setting with  $M = 4$  and Kerr coefficient  $\alpha = 2.2$ , starting from input (3) with  $s = 3$  and  $\eta = 0.04$ . (a) The amplitude and (b) phase structure at  $\zeta = 225$ , obtained starting with the scaled Bessel amplitude  $|b_s| = 0.6$ . The angular velocity is  $\varpi \simeq 0.0267 \pm 0.0003$ , while  $2\eta/s \simeq 0.0267$ . Panels (c) and (d) display the same as (a) and (b), but for  $\alpha = 1.9$  and  $|b_s| = 0.8$ , the angular velocity being  $\varpi \simeq 0.0268 \pm 0.0002$ .

#### IV. STABILITY OF THE DISSIPATIVE AZIMUTHONS

##### A. Stability limits

Similar to nonlinear Bessel vortex beams [20] and dissipatons [21], dissipative azimuthons remain stable for sufficiently low values of the normalized Kerr coefficient  $\alpha$  [see Eq. (11)], and they become unstable above a threshold value,  $\alpha > \alpha_{\text{th}}$ , which is significantly higher than the instability threshold for non-rotating states [20, 21], implying that the rotation enhances the stability. By means of systematic simulations, we have identified the threshold as a function of  $\alpha$  for several values of vorticity  $s$ , using input (13).

Given the large number of parameters, in the numerical simulations we fixed  $|b_s| = 0.6$  and  $|b_s| = 0.8$  [see Eq. (14)], which represent typical intensities at which the Kerr nonlinearity and multiphoton absorption are substantial in fused silica, and  $\eta = 0.04$ , which implies

relative variations of the cone angle  $\simeq 10\%$ .

For  $s = 1$ , the threshold is found to be  $(\alpha_{\text{th}})_{s=1} = 2.25 \pm 0.05$  for  $|b_s| = 0.6$  and  $|b_s| = 0.8$ . The dissipative azimuthons with a higher vorticity are somewhat less stable, featuring  $(\alpha_{\text{th}})_{s=2} = 1.95 \pm 0.05$  for  $|b_s| = 0.6$ , and  $(\alpha_{\text{th}})_{s=2} = 2.15 \pm 0.05$  for  $|b_s| = 0.8$ . Further, for  $s = 3$ , it was found that  $(\alpha_{\text{th}})_{s=3} = 2.25 \pm 0.05$  for  $|b_s| = 0.6$ , and  $(\alpha_{\text{th}})_{s=3} = 1.95 \pm 0.05$  for  $|b_s| = 0.8$ . The difference between the cases of  $s = 2$  and 3 plausibly originates from their differing symmetries. These instability thresholds are about twice as large as typical values  $\alpha_{\text{th}} \simeq 1$  for non-linear Bessel beams and non-rotating dissipatons found in Refs. [20] and [21], respectively, which indicates the enhanced robustness provided by the rotation. Figures 4 and 5 show intensity and phase patterns of the rotating dissipative azimuthons with  $s = 2$  and 3, and  $\alpha = 1$ , which places them well within the stability region.

### B. Instability development scenarios

Direct simulations make it possible to identify two basic scenarios of the development of unstable patterns. Close to the stability boundary, i.e., for the values of  $\alpha$  slightly exceeding  $\alpha_{\text{th}}$ , unstable rotating patterns spontaneously turn into oscillating ones, which keep rotating and may remain robust by themselves. For higher values of  $\alpha$ , an unstable azimuthon decays into random patterns, by progressively losing its symmetry. Three examples of this dynamics are shown in Figs. 6, 7 and 8 for  $s = 1, 2$  and 3, respectively. The instability develops, at first, through a long sequence of regular patterns featuring the same  $2s$ -fold symmetry as the input, which

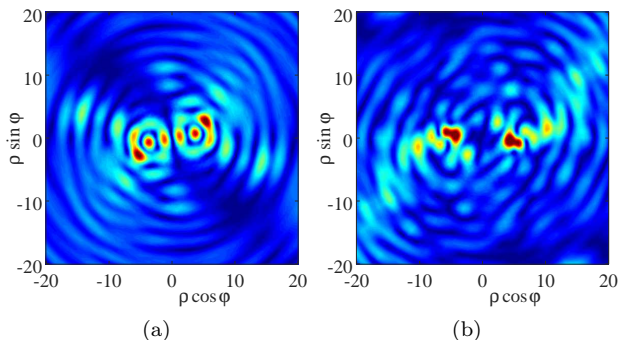


FIG. 6. An example of the instability development, starting from the two-lobe dissipative azimuthon, with  $s = 1$ , and leading to establishment of a random set of isolated hot spots. In this case, the input is similar to that displayed in Fig. 3(c). Examples of a transient regular amplitude pattern, obtained at  $\zeta = 20.625$  (a), and of a random pattern, obtained at  $\zeta = 93.75$  (b). The developing pattern is eventually fully randomized (not shown here). Parameters are  $M = 4$ ,  $\alpha = 4$  for the NLSE, and  $s = 1$ ,  $|b_s| = 0.8$ ,  $\eta = 0.04$  for the Bessel-beam input (3).

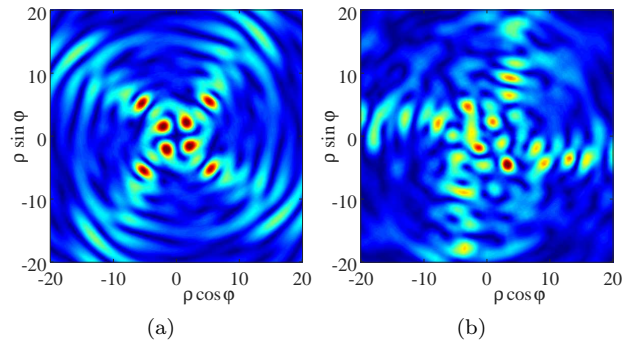


FIG. 7. An example of the instability development, starting from the four-lobe dissipative azimuthon, with  $s = 2$ . In this case, the input is similar to that displayed in Fig. 4(a). Examples of a transient regular amplitude pattern, obtained at  $\zeta = 16.875$  (a), and of a randomized one, established at  $\zeta = 105$  (b). Parameters are  $M = 4$ ,  $\alpha = 4$  for the NLSE, and  $s = 2$ ,  $|b_s| = 0.8$ ,  $\eta = 0.04$  for the Bessel-beam input (3).

follow each other in a random way. Then the pattern becomes less and less regular, developing intrinsic oscillations, until getting complete random.

The instability-development scenario, demonstrated by the numerical solutions, is essentially the same for  $s = 1, 2$  and 3, but the symmetry with respect to the rotation by  $\Delta\varphi = \pi$  for  $s = 1$  is much more robust than the symmetry with  $\Delta\varphi = \pi/2$  for  $s = 2$  or  $\Delta\varphi = \pi/3$  for  $s = 3$ . The patterns for  $s = 1$  are much simpler, and, typically, the resulting random structure still keep the symmetry with respect to the rotation by  $\Delta\varphi = \pi$  [see, e.g., Fig. 6(b)].

The phase pattern globally reflects the shape of the in-

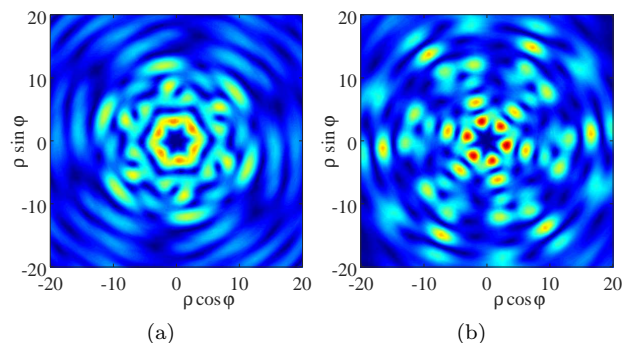


FIG. 8. Examples of the instability development of the six-lobe dissipative azimuthon, proceeding through a sequence of regular patterns, the input pattern being close to that shown in Fig. 5(a), while the final pattern (not shown here) is a random set of isolated hot spots. Examples of transient regular patterns are displayed at (a)  $\zeta = 7.5$  and (b)  $\zeta = 13.125$ . Parameters are  $M = 4$ ,  $\alpha = 4$  for the NLSE, and  $s = 3$ ,  $|b_s| = 0.8$ ,  $\eta = 0.04$  for the Bessel-beam input.

tensity pattern. However, if one considers the phase as a function of azimuthal angle  $\varphi$  along circumferences with different radii  $\rho$ , conspicuous evolution in the course of the evolution in  $\zeta$  can be identified. Indeed, while the phase circulation is  $2\pi s$  in the core of the input configuration (3), and  $-2\pi s$  just after the topological charge has reversed its sign, a central domain of small radius in which the phase circulation is zero quickly emerges in the course of the evolution of the unstable azimuthon. The radius of this domain grows until it fills the entire core of the pattern, except for a few remaining phase dislocations, whilst the pattern becomes random. Thus, the evolution leads to a conclusion that the core area of the pattern does not carry vorticity anymore. Alternations of domains with phase circulations  $2\pi s$  and  $-2\pi s$  still occurs at different increasing values of the radius and, as expected, in the peripheral area (at large radii) the alternations become identical to that of the input Bessel-beam superposition.

### C. Pulsating and breathing dissipative azimuthons

In the case of vorticity  $s = 2$ , a peculiar instability scenario exhibits spontaneous transition of the four-lobe pattern into a two-lobe one. The development of this scenario is quite slow, allowing the initial four-lobe pattern to propagate considerable distances, keeping an apparently stable shape. The transition commences with oscillations of the amplitude of two pairs of hot spots which constitute the cross (four-lobe) structure of the input. Such oscillations may lead directly to the destruction of the structure, or proceed in an apparently persistent way. Due to a limited propagation distance in the simulations and very low instability growth rate, it is not always possible to distinguish these outcomes. An example is produced in Fig. 9 for  $s = 2$ ,  $|b_s| = 0.8$ , and  $\alpha = 2.6$ , in which the emerging oscillatory state appears to be stable. In this case, input (3) quickly forms a dissipative azimuthon, that propagates without any visible instability up to  $\zeta \simeq 75$ . Then, amplitudes of the lobes start to oscillate until the pattern reshapes into a fully robust two-lobe structure.

Another noteworthy propagation regime triggered by the instability for  $s = 1$  is the formation of a permanently breathing dissipative azimuthon. As seen in Fig. 10, in this case oscillations occur between a pattern in which the hot spots with the largest amplitude are closest to the center [Fig. 10(a)], and another one, in which the hot spots are located on a secondary ring [Fig. 10(b)]. This regime sets in as a persistent one, after a transient stage in which the intensity maxima of the farther separated spots are lower. The dynamics of the breathing dissipative azimuthon is displayed in Supplemental Material [URL of Fig10.avi].

There is also a dynamical regime exhibiting spontaneous transformation of a transient oscillatory state, which keeps a high level of symmetry, into another one

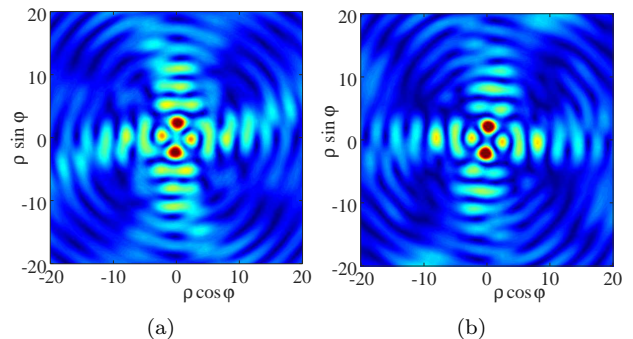


FIG. 9. An example of the formation of a pulsating dissipative azimuthon, triggered by the instability of a four-lobe azimuthon. In this case, input (3) is similar to that in Fig. 4. (a) At  $\zeta = 115.625$ , the instability has just led to the appearance of a two-lobe pattern. (b) A snapshot of a persistent oscillatory pattern at  $\zeta = 231.25$  [it has rotated by  $\Delta\varphi = \pi/2$  between (a) and (b)]. Parameters are  $s = 2$ ,  $M = 4$ ,  $\alpha = 2.6$ ,  $|b_s| = 0.8$ , and  $\eta = 0.04$ .

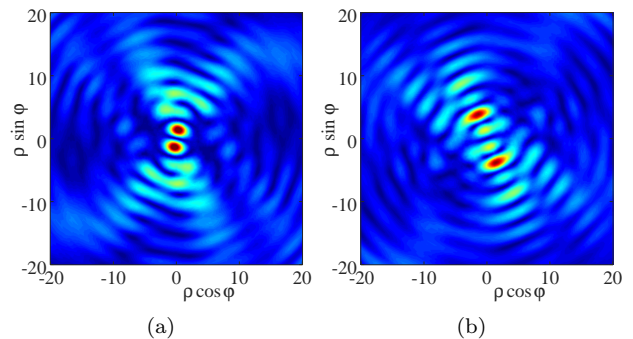


FIG. 10. A breathing dissipative azimuthon. It oscillates between two configurations: at  $\zeta = 193.75$  (a) and 200 (b), the major amplitude maxima are located, respectively, at internal and external positions. Parameters are  $s = 1$ ,  $M = 4$ ,  $\alpha = 3$ ,  $|b_s| = 0.6$ , and  $\eta = 0.04$ . See Supplemental Material [URL of Fig10.avi] for a detailed picture of the breathing-azimuthon dynamics.

with a lower symmetry, as shown in Fig. 11. The initial six-lobe azimuthon is similar to the one displayed Fig. 5 but for a larger scaled strength of the Kerr non-linearity,  $\alpha$  [see Eq. (11)]. At the first, relatively long, stage of the evolution ( $\zeta \lesssim 75$ ), the pattern remains unchanged in the rotating reference frame, before the instability commences. Then, the first oscillatory state emerges, see Figs. 11(a) and (b), which keeps essential symmetry: the initial invariance with respect to the rotation by  $\Delta\varphi = \pi/3$  is lost, being reduced to the invariance with  $\Delta\varphi = \pi$ , but the axial symmetry is conserved. The amplitude oscillates between configurations with two opposite spots and four spots. Then, the structure switches into a second oscillatory state, which keeps solely the



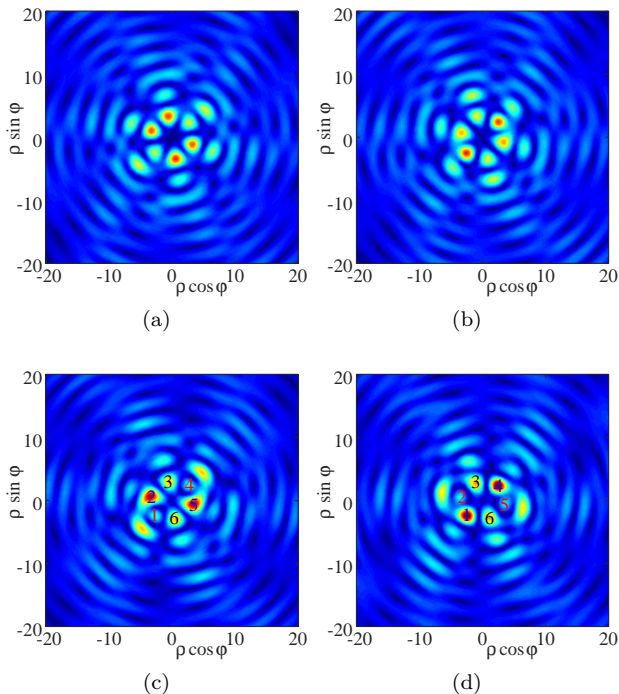


FIG. 11. An example of the unstable evolution of the six-lobe dissipative azimuthal mode. The respective input (3) is similar to that presented in Fig. 5. At the first stage of the evolution, the pattern oscillates between configurations shown in (a), at  $\zeta = 125$ , and (b), at  $\zeta = 128.125$ . At the second stage, the pattern oscillates between the configurations shown in (c), at  $\zeta = 165.625$ , and (d), at  $\zeta = 168.750$ . Parameters are  $s = 3$ ,  $M = 4$ ,  $\alpha = 3$ ,  $|b_s| = 0.6$ , and  $\eta = 0.04$ .

symmetry with respect to the rotation by  $\Delta\varphi = \pi$ , see Figs. 11(c) and (d). In this state, oscillations occur between opposite spots in two pairs, labeled (1, 4) and (2, 5) in the figure, while the spots belonging to the third pair, (3, 6), keep a low intensity. Note that the apparent rotation by  $\pi/6$ , which relates Figs. 11(c) and (d), is actually a consequence of the oscillations. Indeed, the rotation angle per se between the configurations in panels (c) and (d), separated by propagation distance  $\Delta\zeta = 3.125$ , is  $\Delta\varphi = \varpi\Delta\zeta = (2\eta/s)\Delta\zeta$  [see Eq. (15)], which yields  $\Delta\varphi = 4.77^\circ$ .

## V. CONCLUSION

We have reported the existence of a novel type of azimuthal modes, which represent the propagating optical field with a stationary intensity pattern in a uniformly rotating reference frame in the Kerr medium with nonlinear loss, induced by multiphoton absorption in the material. Similar to nonlinear Bessel fundamental [13, 14] and vortical [17, 20] beams and “dissipators” [21], the steady propagation of the rotating azimuthal modes in the

lossy medium is maintained by the flux from the peripheral reservoir, which stores an indefinitely large amount of power in the slowly decaying tails of the beam. Unlike conservative azimuthal modes [5, 6], the number  $N$  of “hot spots” (intensity maxima) and the vorticity of the input are linked by  $N = 2s$ , rather than being mutually independent.

The rotating dissipative azimuthal modes are excited by the coherent superposition of two Bessel beams with opposite topological charges and slightly different cone angles, cf. Refs. [24, 25]. In comparison to the non-rotating intensity patterns excited by the Bessel-beam pairs with identical conicities, the rotating azimuthal modes form faster and are more robust. The existence and stability of these modes in the self-focusing Kerr medium is provided by the nonlinear absorption. If the absorption is turned off, the input superposition of the Bessel beams does not result in formation of any stationary pattern. Unstable rotating azimuthal modes in this model are interesting objects too, because the development of the instability gives rise to various dynamical regimes, including persistently pulsating and breathing azimuthal modes, as well as the transition to “turbulent” patterns.

These results may help to understand physics underlying the recently observed helical filaments, excited by superpositions of Bessel-Gauss beams with opposite vorticities in air and  $\text{CS}_2$  [22, 23], where the interplay of the Kerr nonlinearity and multiphoton absorption, induced by ionization of air, plays a key role in the propagation.

## ACKNOWLEDGEMENTS

M.A.P. acknowledges funding by Spanish Ministerio de Economía y Competitividad, grant No. PGC2018-093854-B-I00 and No. FIS2017-87360-P. B.A.M. appreciates support from the Israel Science Foundation, through grant No. 1286/17.

## Appendix: Numerical schemes

The validity of all the numerical results reported above has been verified by running the simulations independently in the Cartesian and polar coordinates, by means of different algorithms, with different discretization meshes. In the former case, a standard symmetrized split-step Fourier method applied to the rectangular mesh, using the fast Fourier transform to perform linear steps of the integration, and a trapezoidal method for the nonlinear steps. With the polar coordinates, a 5-points finite-difference scheme was employed to evaluate the transverse derivatives, and a 4th-order Runge-Kutta scheme for the axial integration on the polar mesh. It has been concluded that all the results produced by means of both coordinates systems are identical.

Special boundary conditions were required to simulate the propagation of Bessel-beam superpositions with tails

slowly decaying at  $r \rightarrow \infty$ . In all the simulations, the evolving field was set equal to the linearly propagated field, whose analytical expression is given by Eq. (5), in a narrow strip attached to the transverse computational boundary, which contains a few radial points of the discretization mesh. From the physical point of view, these boundary conditions are justified as the propagation of the small-amplitude tails is initially linear, and the boundary conditions emulate the divergence of the total

power in the reservoir. On the computational side, the same boundary conditions initially eliminate unphysical inward-propagating boundary waves, that would emerge if zero boundary conditions were used. Results of the simulations become invalid at values of the propagation distance at which nonlinear excitations propagating from the high-intensity beam's core outwards are reflected at the strip boundary and come back to the core.

- 
- [1] A. S. Desyatnikov, L. Torner, Y. S. Kivshar, "Optical vortices and vortex solitons," *Progr. Opt.* **47**, 291–391 (2005).
- [2] B. A. Malomed, "Vortex solitons: Old results and new perspectives," *Physica D: Nonlinear Phenomena* **399**, 108–137 (2019).
- [3] A. S. Desyatnikov, A. A. Sukhorukov, and Yu. S. Kivshar, "Rotating Optical Soliton Clusters," *Phys. Rev. Lett.* **88**, 053901 (2002).
- [4] Y. V. Kartashov, B. A. Malomed, V. A. Vysloukh, M. R. Belić, and L. Torner, "Rotating vortex clusters in media with inhomogeneous defocusing nonlinearity," *Opt. Lett.* **42**(3), 446–449 (2017).
- [5] A. S. Desyatnikov, A. A. Sukhorukov, and Yu. S. Kivshar, "Azimuthons: spatially modulated vortex solitons," *Phys. Rev. Lett.* **95**, 203904 (2005).
- [6] A. Minovich, D. N. Neshev, A. S. Desyatnikov, W. Krolikowski, and Y. S. Kivshar, "Observation of optical azimuthons," *Opt. Express* **17**, 23610 (2009).
- [7] Y. Kartashov, G. Astrakharchik, B. Malomed, and L. Torner, "Frontiers in multidimensional self-trapping of nonlinear fields and matter," *Nature Reviews Physics* **1**, 185–197 (2019).
- [8] Y. V. Kartashov, B. A. Malomed, and L. Torner, "Metastability of quantum droplet clusters," *Phys. Rev. Lett.* **122**, 193902 (2019).
- [9] N. Akhmediev and A. Ankiewicz (Eds.), *Dissipative Solitons*, *Lect. Notes Phys.* **661** (Springer, Berlin Heidelberg 2005).
- [10] N. A. Veretenov, N. N. Rosanov, and S. V. Fedorov, "Rotating and precessing dissipative-optical-topological-3D solitons," *Phys. Rev. Lett.* **117**, 183901 (2016).
- [11] N. A. Veretenov, S. V. Fedorov, and N. N. Rosanov, "Topological vortex and knotted dissipative optical 3D solitons generated by 2D vortex solitons," *Phys. Rev. Lett.* **119**, 263901 (2017).
- [12] T. Mayteevarunyoo, B. Malomed, and D. Skryabin, "Vortex modes supported by spin-orbit coupling in a laser with saturable absorption," *New J. Phys.* **20**, 113019 (2018).
- [13] M. A. Porras, A. Parola, D. Faccio, A. Dubietis, and P. Di Trapani, "Nonlinear Unbalanced Bessel Beams: Stationary Conical Waves Supported by Nonlinear Losses," *Phys. Rev. Lett.* **93**, 153902 (2004).
- [14] P. Polesana, A. Dubietis, M. A. Porras, E. Kucinskas, D. Faccio, A. Couairon, and P. Di Trapani, "Near-field dynamics of ultrashort pulsed Bessel beams in media with Kerr nonlinearity," *Phys. Rev. E* **73**, 056612 (2006).
- [15] P. Polesana, M. Franco, A. Couairon, D. Faccio, P. Di Trapani, "Filamentation in Kerr media from pulsed Bessel beams," *Phys. Rev. A* **77**, 043814 (2008).
- [16] A. Couairon, A. Mysyrowicz, "Femtosecond filamentation in transparent media", *Phys. Rep.* **441**, 47–189 (2007).
- [17] M. A. Porras and C. Ruiz-Jiménez, "Nondiffracting and nonattenuating vortex light beams in media with nonlinear absorption of orbital angular momentum," *J. Opt. Soc. Am. B* **31**, 2657 (2014).
- [18] V. Jukna, C. Milin, C. Xie, T. Itina, J. Dudley, F. Courvoisier, and A. Couairon, "Filamentation with nonlinear Bessel vortices," *Opt. Express* **22**, 25410 (2014).
- [19] C. Xie, V. Jukna, C. Milin, R. Giust, I. Ouadghiri-Idrissi, T. Itina, J. M. Dudley, A. Couairon, and F. Courvoisier, "Tubular filamentation for laser material processing," *Scientific Reports* **5**, 8914 (2015).
- [20] M. A. Porras, M. Carvalho, H. Leblond, and B.A. Malomed, "Stabilization of vortex beams in Kerr media by nonlinear absorption," *Phys. Rev. A* **94**, 053810 (2016).
- [21] M. A. Porras, C. Ruiz-Jiménez, and M. Carvalho, "Stationary and stable light-beam propagation in Kerr media with nonlinear absorption with controllable dissipation patterns," *Phys. Rev. A* **95**, 043816 (2017).
- [22] N. Barbieri, Z. Hosseinimakarem, K. Lim, M. Durand, M. Baudelet, E. Johnson, and M. Richardson, "Helical filaments," *Appl. Phys. Lett.* **104**, 261109 (2014).
- [23] J.-q. Lü, P.-P. Li, D. Wang, C. Tu, Y. Li, and H.-T. Wang, "Control on helical filaments by twisted beams in a nonlinear CS<sub>2</sub> medium," *Opt. Express* **26**, 29527 (2018).
- [24] R. Vasilyeu, A. Dudley, N. Khilo, and A. Forbes "Generating superpositions of higher-order Bessel beams," *Opt. Express* **17**(26), 23389–23395 (2009).
- [25] R. Rop, A. Dudley, C. López-Mariscal, and A. Forbes "Measuring the rotation rates of superpositions of higher-order Bessel beams," *J. Mod. Opt.* **59**(3), 259–267 (2012).
- [26] M. A. Porras, I. Gonzalo, and R. Weigand, "Optical rotation of a uniformly, linearly polarized Bessel-like beam in free space," *Opt. Soc. Am. A* **33**, 2061–2065 (2016).
- [27] P. Johansson, D. Anderson, M. Lisak, and M. Marklund, "Nonlinear Bessel beams," *Opt. Commun.* **222**, 107–115 (2003).
- [28] T. J. Alexander, A. A. Sukhorukov, and Y. S. Kivshar, "Asymmetric vortex solitons in nonlinear periodic lattices", *Phys. Rev. Lett.* **93**, 063901 (2004).
- [29] A. Bezryadina, E. Eugenieva, and Z. Chen, "Self-trapping and flipping of double-charged vortices in optically induced photonic lattices", *Opt. Lett.* **31**, 2456–2458 (2006).